Design, Fabrication and Initial Results of a 2g Autonomous Glider

R. J. Wood[1], S. Avadhanula[1], E. Steltz[1], M. Seeman[1], J. Entwistle[1], A. Bachrach[1], G. Barrows[2], S. Sanders[1], and R. S. Fearing[1,3]

[1]University of California, Berkeley, CA 94720
[2]Centeye, Inc., Washington, DC 20005
[3]ronf@eecs.berkeley.edu
http://robotics.eecs.berkeley.edu/∼ronf/uglider

Abstract— **Utilizing the core technologies of emerging microrobotic structures, the rapid design and prototyping of a passive micro air vehicle with the final goal of locating an audio source while avoiding hazardous obstacles is presented. The airfoil and control surfaces are optimized empirically to maximize lift and maneuverability while minimizing drag. Bimorph piezoelectric bending cantilevers actuate the control surfaces. Since such actuators require high voltages, an efficient boost circuit is presented along with appropriate high voltage electronics. To locate audio sources, a pair of acoustic sensors is designed and prototyped using a phase detection algorithm while a custom optic flow sensor is developed to avoid obstacles and give estimates of object distances and velocities. Finally, each subsystem is demonstrated and the complete glider is integrated to demonstrate initial open loop control performance.**

I. Introduction

There is a large body of existing and emerging research on various classes of micro air vehicles (MAVs). Such devices can be loosely defined as existing on a scale of approximately 15cm, and generally less than 100g. There is a large range of applications appropriate for MAVs such as reconnaissance, hazardous environment exploration, and search and rescue. MAVs may broken into a number of classes such as fixed wing ([9], [11], [13], [16]) flapping wing ([3], [4], [7], [14], [15], [20]), or rotary wing. One area which has remained somewhat sparse is passive MAVs. This paper explores the design, fabrication, and results for a palm-sized autonomous glider. Fig. 1 shows the most recent version of the MicroGlider.

A primary concern in designing this MAV is the power and mass budget allotted to each component. Shown in Tab. I are the preliminary estimates and measurements for each subsystem.

II. Airfoil, Fuselage and Control Surfaces

The first consideration in the design of a micro air vehicle is the optimization of the lift producing and control surfaces and support structures. In addition, it is of great use to develop a flight simulator to estimate the performance of the MAV for various morphological and environmental changes.

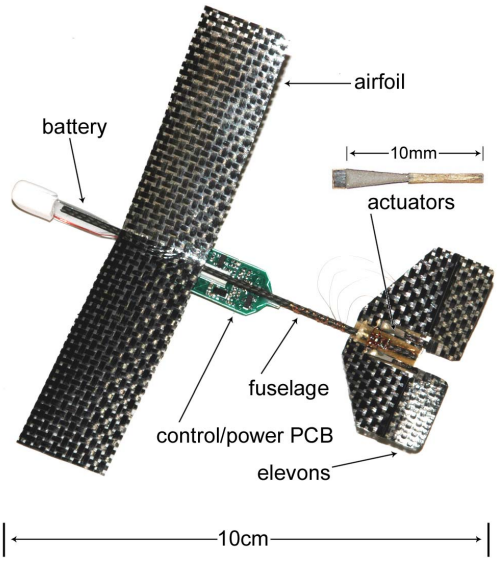

Fig. 1. Complete 2g MicroGlider.

TABLE I
Preliminary mass and power budgets.

Subsystem	mass (mg)	power (mW)
airfoil	265	—
fuselage	130	—
control surfaces	100	—
elevons	50	—
actuators	50	4
control/power PCB	440	—
H.V. electronics	—	3
control electronics	—	5
optic flow	325	29
acoustic[1]	200	5
battery	700	—
total	2220	46

[1]goal specifications

A. Airfoil

The airfoil consists of a molded composite surface. The optimal geometric airfoil properties are determined via em-

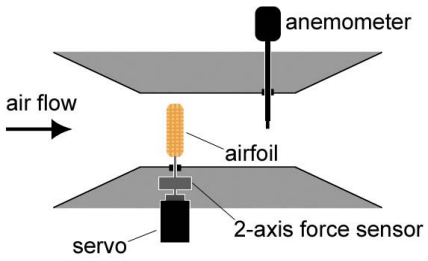

Fig. 2. Wind tunnel airfoil measurement setup.

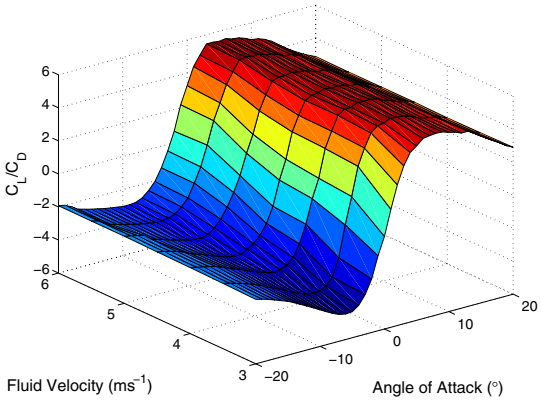

Fig. 3. Lift and drag coefficients for a sample airfoil.

pirical lift and drag measurements. Initially, airfoil geometric parameterization is chosen based upon computational fluid dynamic (CFD) modeling. Key parameters of the airfoil include aspect ratio (AR), chord length (l_c), camber percentage, and position of maximum camber. From the CFD analysis, a sample of these parameters are chosen and the appropriate airfoils are created via a composite molding process [17].

Each chosen airfoil is attached to a custom two axis force sensor capable of measuring normal and tangential forces with a resolution of approximately 10μN. This system is fitted to a wind tunnel on a servo capable of sub-degree resolution rotations (see Fig. 2). The wind tunnel air velocity and the servo angle are controlled via xPC (from MathWorks). An anemometer measures the air velocity such that the precise wind speed may be regulated via a traditional feedback control system. The lift and drag coefficients are then measured as a function of both fluid velocity and angle of attack. Sample results are shown in Fig. 3.

B. Control Surfaces

For simplicity, the control surface morphology is a split tail configuration. Two surfaces, called elevons, map two actuator inputs to roll, pitch, and yaw body torques. The elevons are actuated via piezoelectric bending actuators [18] and require an amplifying transmission system as will be discussed in this section.

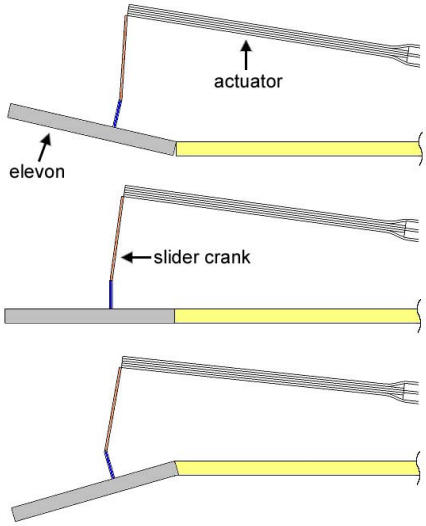

Fig. 4. Detail of elevon transmission system.

B.1 Elevon Kinematics and Dynamics

The elevon, actuator, and control surface form a closed parallel chain via an additional laser-micromachined link. The distal end of the actuator is connected to the elevon hinge via a slider-crank to form a four bar mechanism (similar to the mechanism in [17]) as is shown in Fig. 4. Thus the small displacement of the actuator is amplified into a larger rotation at the base of the elevon.

The forward kinematics for such a chain are determined by the relative lengths of the constituent members [19] and is given as follows:

$$\alpha_e = \pi - \left(\cos^{-1}\left(\frac{z^2 + l_1^2 - l_2^2}{2 z l_4} \right) \pm \cos^{-1}\left(\frac{z^2 + l_4^2 - l_3^2}{2 z l_4} \right) \right) \tag{1}$$

where α_e is the elevon angle, l_1, l_2, l_3, and l_4 are the lengths of the control surface, actuator, connector rod, and elevon attachment respectively, and $z = \left(l_1^2 + l_2^2 - 2 l_1 l_2 \cos\left(\alpha_{in}\right)\right)^{\frac{1}{2}}$. Thus the amplification of the actuator motion can be selected based upon the relative geometries. An example of this is shown in Fig. 5. In this figure, $\pm 200\mu$m of actuator motion yields $\pm 2^\circ$ of elevon deflection. To determine if this is sufficient to achieve the desired level of maneuverability, elevon forces are measured and transformed into torques via a simplified rigid body model of the MicroGlider.

B.2 Glider Torque Map

Due to power and mass limitations, the processing power of the MicroGlider controller will be significantly less than that of traditional robotic systems. This places limits on the fidelity of control. One solution to this problem is to characterize the body torques produced by various control inputs and choose appropriate spaces in this map to generate independent body torques in a discrete manner. The first step in this process is to model the overall system via

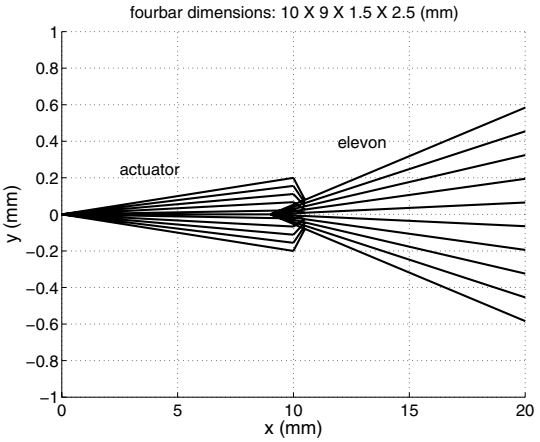

Fig. 5. Sample kinematics for the control surfaces. The lines represent the four constituent elements of the kinematic chain.

the following mapping:

$$\begin{bmatrix} s_l \\ s_r \end{bmatrix} \xrightarrow{T} \begin{bmatrix} \tau_r \\ \tau_p \\ \tau_y \end{bmatrix} \tag{2}$$

where the subscripts r, p, and y represent roll, pitch, and yaw with respect to the body moments about the center of gravity (CG) and s_l and s_r are the left and right control signals. Ideally, this map would be measured directly as a two input, three output system using a three axis torque sensor while spanning the appropriate space of the two input voltages. This is impractical since existing multi axis torque sensors are either too insensitive ($>>$ 10mN·mm resolution), have insufficient bandwidth ($<$ 100Hz), or are simply too bulky to be placed in the wind tunnel with the glider. As an alternate approach, the individual elevon lift and drag forces are measured using a similar setup as with the airfoil optimization. In this setup, a single elevon is rigidly attached to the two-axis force sensor and the lift and drag are measured as a function of the actuator input voltage. In addition, the elevon angle of attack can be altered to give a two-input, two-output map to simulate the forces experienced during side slip. However for these initial results it will be assumed that there is no slip (i.e. the glider body axis is always parallel with the direction of fluid flow). Note that this is done at the optimal fluid velocity as determined by the airfoil tests. Now the following mapping can be described:

$$[s] \xrightarrow{T_s} \begin{bmatrix} F_{\text{lift}} \\ F_{\text{drag}} \end{bmatrix} \tag{3}$$

This map can be used to develop the final mapping (equ. 2) through the glider geometry. An example of this map is shown in Fig. 6.

Now let θ, l_e, and l_f represent the elevon dihedral angle, the distance from the fuselage to the individual elevon center of pressure, and the length from the CG to the elevon center of pressure respectively (see Fig. 7). Thus, a simplified map from elevon lift forces to body torques can be

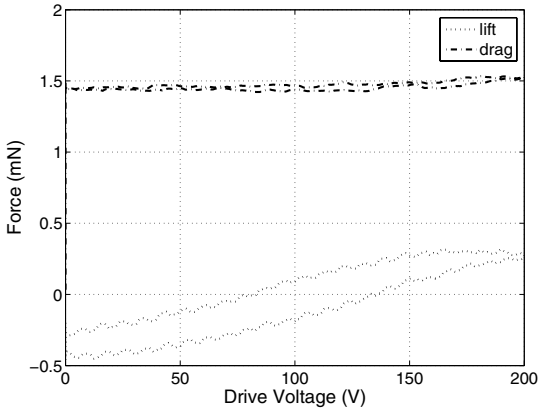

Fig. 6. Elevon lift and drag measurements as a function of actuator voltage. Note that the drag is relatively independent of the applied voltage.

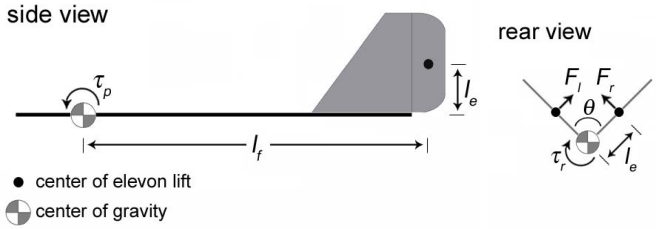

Fig. 7. Simplified glider drawing showing rigid body geometric parameters.

derived and is shown in the following:

$$\begin{bmatrix} \tau_r \\ \tau_p \\ \tau_y \end{bmatrix} = \begin{bmatrix} l_e & -l_e \\ l_f \sin(\theta/2) & l_f \sin(\theta/2) \\ l_f \cos(\theta/2) & -l_f \cos(\theta/2) \end{bmatrix} \begin{bmatrix} F_l \\ F_r \end{bmatrix} \tag{4}$$

where F_l and F_r are the elevon lift forces from equ. 3 for the left and right elevon respectively (again, see Fig. 7). Note again that since the elevon drag forces are constant, they are a static disturbance and will not be considered in the formulation of the body torques. Finally, these two maps are combined (along with linearized elevon lift data from Fig. 6) to give the desired map T and this is shown in Fig. 8 for all three body torques. Subsections of this map are used by the flight control system to perform appropriate maneuvers during flight.

C. Fuselage and Fabrication

The airfoil, control surfaces, and fuselage each consist of composite materials. This gives great versatility to the manufacturing process since unidirectional or woven lamina of these materials are easily molded. In addition, the composites are initially in a form called prepreg which consists of sheets of bundled fibers impregnated with a catalyzed but uncured epoxy. The epoxy inherent in these lamina negates the need for additional bonding layers when forming more complex structures. The airfoil is cut as a prepreg and compression molded while curing to give the desired cross section. The control surfaces are also cut as prepreg and are fixed in a mold with the cylindrical carbon fiber

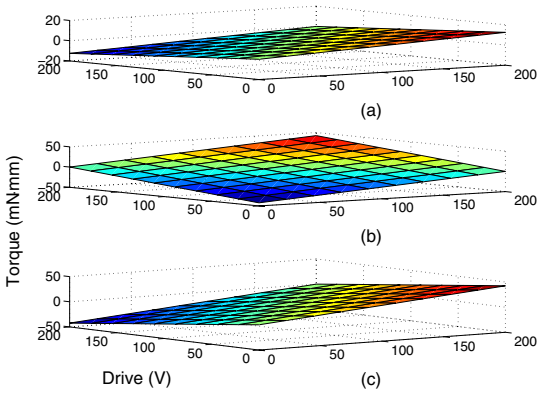

Fig. 8. Roll (a), pitch (b), and yaw (c) torques as a function of the two elevon inputs.

fuselage and cured. The elevons are fixed to the control surface via laser-micromachined links and hinges to form the elevon transmission. Finally, the actuators are fixed to the control surfaces and wired by hand.

D. Simulation

In order to assist in design and testing, a software tool has been developed in order to accurately simulate the MicroGlider in flight. This simulator is being used to quickly evaluate body design changes to the MicroGlider and their effects in a virtual environment. In addition, the use of the simulator to test the performance of different flight control algorithms has begun.

The simulator is a 3-axis, 6 degree of freedom simulator implemented in Matlab. The simulator combines classic rigid body dynamics with empirically measured MicroGlider parameters to calculate the state of the system during a virtual flight. The model parameters used in the simulator include the mass and inertial matrix of the MicroGlider, the size and position of various glider components, as well as the lift and drag coefficients of the wings, body, and elevons. These parameters can be modified to analyze their effects and maximize flight performance.

The simulator is broken up into two primary modules. The first module takes the current state of the system and calculates the forces due to aerodynamic effects. The second module uses those forces as well as geometric parameters to continually update the state of the MicroGlider.

In addition to simulating the trajectory of the MicroGlider, the simulator is used to estimate the sensor response for various sensor configurations, as well as different simulated environments. This allows the user to evaluate what the MicroGlider perceives, and to utilize this information to design superior control strategies. Currently this is limited to photodiode inputs from environmental light sources. Eventually, the sensor module may include virtual models for optic flow sensors, microphones, and possibly gyroscopes and accelerometers.

As an example of the simulator functionality, Figs. 9 and 10 show the predicted response to two typical flight modes.

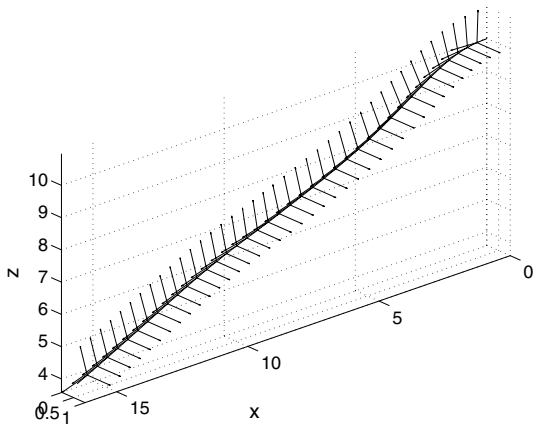

Fig. 9. Simulated MicroGlider reaching steady glide slope after initial horizontal launch. Position is shown every tenth of a second, using the body coordinate system of the glider.

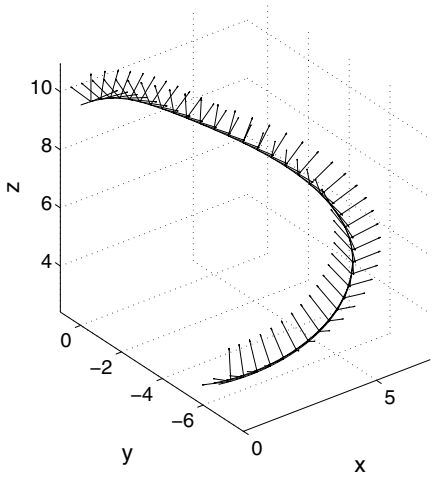

Fig. 10. Simulated MicroGlider executing a steady turn to the right after initial horizontal launch.

III. Control and Power Electronics

As seen in Fig. 1, the electronics and control reside on a discrete PCB mounted to the center portion of the fuselage. This board performs all control tasks, collaborates sensing and communication, conditions the battery power, protects the battery with low voltage detection, and contains the high voltage electronics required to drive the actuators. Fig. 11 displays an overview of the electronics contained on this PCB. The power for the MicroGlider is supplied by a single 20mAh Lithium Polymer (LiPo) battery. This chemistry allows very high discharge rates (>5C) and can thus yield approximately 400mW for 10min flight durations. The conditioning and boosting of this battery voltage will be first discussed in this section proceeded by appropriate control circuitry for the high voltage electronics and processing of the sensor inputs.

A. Introduction

The control PCB must be able to monitor all on-board sensors while steering the elevons appropriately. Addition-

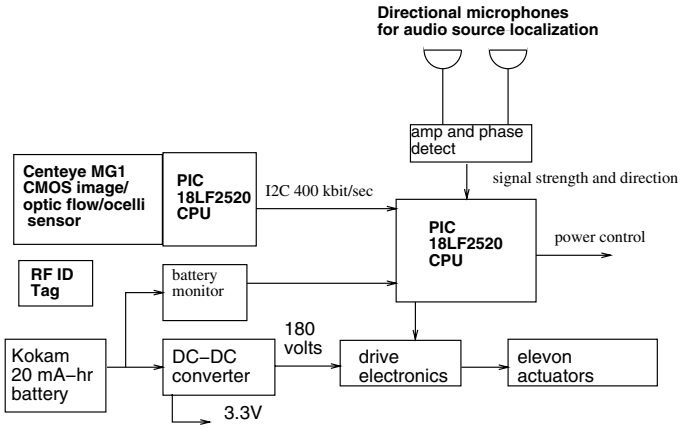

Fig. 11. Block diagram of glider electronics and control.

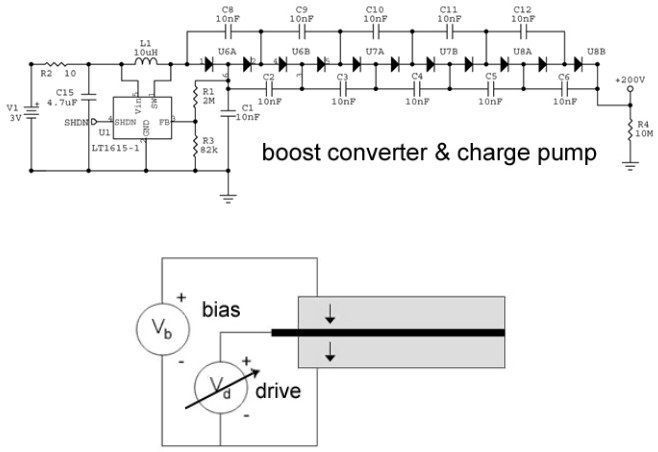

Fig. 12. Schematic of DC-DC converter (a) and dual-source bimorph drive scheme (b).

ally, the board must be lightweight and consume very little power so that the lifetime of the glider is sufficient.

Several commercially available control boards were considered, including products by Softbaugh (part number T1121, 1.7g) or Didel (for example WdPicDev84). However, the MicroGlider requires a board under 500mg including high voltage electronics. Since the MicroGlider will employ piezoelectric actuators, some type of power amplifier to boost the battery voltage to 200 volts is required for use. No such board has been found that meets these specifications.

Other researchers have constructed custom piezoelectric microrobot control boards, such as Brufau et al's MICRON control board [6] and Montane et al [10]. However, most of these boards are meant to drive piezoelectric stack actuators, which require voltages much lower than the MicroGlider's cantilever actuators (≈20-50V for stack actuators vs 200V for the bimorphs used here). Therefore, a custom control and power board was created to satisfy these needs.

B. Power Electronics

The bimorph piezoelectric actuators require both a high-voltage bias supply (V_b) and a signal (V_d)ranging between ground and V_b to create displacement (see [18] for details on drive method). To minimize weight, a pulse-width modulated n-channel MOSFET in series with a pair of resistors is used to modulate the bias supply. A 10MΩ resistor is used to charge the actuator and a 2MΩ resistor is used to discharge the actuator. The time constant associated with the actuator's capacitance and these series resistors filters out the PWM square wave to create the desired low-frequency waveform.

B.1 Piezo Bias DC-DC Converter

The piezoelectric actuators used here require 200V to provide adequate deflections [18]. Many solutions exist for obtaining this from low voltages, but none are optimized for weight. Based on the minimal amount of power needed and the stringent weight requirement, a number of converter designs were investigated.

Based on component packages easily obtainable, the majority of the converter weight was comprised of the inductor and control electronics. A custom IC is not currently feasible due to expense and lead time. A specialized low-power boost converter IC (Linear Technology LTC1615-1) is used for the control electronics and active power switch. This topology (Fig. 12) uses a simple inductor rather than a heavier transformer.

The boost converter outputs 30 volts, just under the limit of the LTC1615 part. A pulsed waveform (ranging between zero and 30 volts) is formed across the boost converter diode. The charge-pump multiplies this voltage by a factor of 7 (ideally) to produce the bias voltage. Although the charge pump involves a number of capacitors and diodes, its weight is minimized through the use of 0402 capacitors and multi-diode surface-mount components. When built, the converter outputs 160V when driven from a 3.5V source. Over the expected operating range (2.5 to 8 mW output power), the converter is between 51 and 63 percent efficient. These losses are attributed to the quiescent power draw and switching loss of the boost converter IC. The DC output impedance is 48.2 kΩ and the bandwidth is 3Hz. The converter's components weigh approximately 120 milligrams, neglecting the PCB weight, and occupy 70 square millimeters of board space (with components on both sides).

C. Control Electronics

The chosen processor for the MicroGlider is the Microchip PIC 18LF2520. This processor was chosen for its internal oscillator, low power consumption, and small outline (28 pin QFN package, approximately 90 mg). The microcontroller also has two PWM outputs (to drive the two elevon MOSFETs) and several A/D converters to measure sensors on the board. Additionally, the microcontroller interfaces well via the I2C protocol to the optic flow sensor as (as discussed in section IV-C).

A further feature of the control board is its ability to accommodate a variety of sensors (the entire board is shown

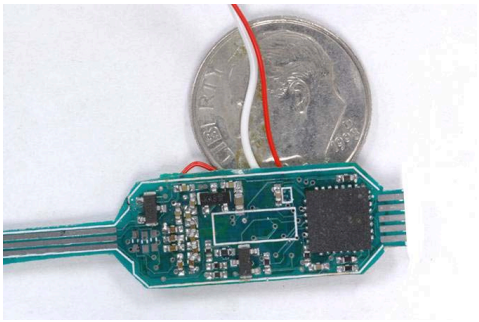

Fig. 13. MicroGlider power/control board (top side).

in Fig. 13). There is a flexible ribbon cable coming off the board to attach to the elevon actuators and also to another sensor (in addition to the audio sensor on the main board), which could be a microphone or phototransistor/diode for example. It also contains a double DIP switch for master on/off and another digital input that is software customizable. The board can easily be programmed via a ZIF connector at one end of the board. The total weight of this populated PCB is 440mg, and it consumes about 12.85mW (driving actuators and running a program at 1 MIPS).

IV. Sensors and Navigation

Navigation for the MicroGlider is expected to primarily be based on audio sensing via two microphones placed at the front and aft of the aircraft. The final aim is that once the MicroGlider is released approximately pointing toward a sound source, it can home in onto the sound source and land as close to it as possible. An optic flow sensor placed toward the front of the glider will aid in obstacle avoidance during this process. The overall flight scheme is thus a combination of audio based navigation and optical obstacle avoidance.

Audio based navigation can be roughly viewed at two levels: the low level audio localization part and the higher level navigation part. In the following sections, we first describe our algorithm for sound localization followed by the higher level navigation scheme.

A. Sound Localization

Many methods have been reported for sound source localization involving Fourier transforms, time frequency histograms [2], multiple (more than two) microphones [12] etc. In the current implementation, the system is limited to two on-board microphones. Moreover, the simplicity of the on-board processor demands that the method not be computationally intensive and not interfere with other flight control. Thus ideally the algorithm should be implemented in analog or digital hardware as much as possible to eliminate CPU computation.

The sound signals detected by the two microphones are fed into two hardware phase locked loops (PLLs). The voltage controlled oscillator output of each PLL is a pulse train phase locked to the input sound signal. This works well since the sound signal to be detected is expected to be narrow-band. The two slightly out of phase pulse trains

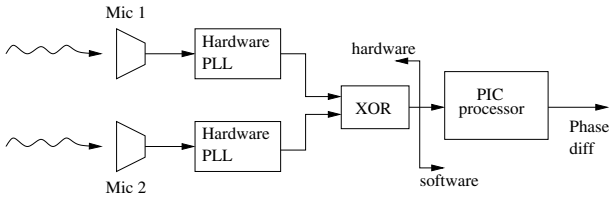

Fig. 14. Algorithm for detecting phase between two microphones.

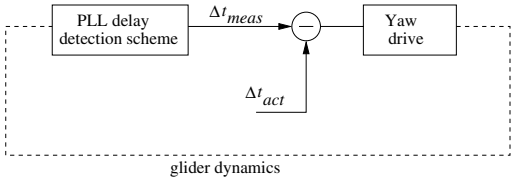

Fig. 15. Far field navigation scheme.

are fed into a hardware XOR gate, which goes high whenever the two pulse trains differ in value. By measuring the duration for which the XOR gate is high, the duration for which the two pulse trains have differing values can be calculated. Since the pulse trains are phase locked to the incoming sound signals, the duration for which the XOR gate is high is directly proportional to the phase difference of the two incoming sound signals. A block diagram of this audio localization method appears in Fig. 14. Once the phase difference is calculated it can be used directly as an input for higher level navigation control.

B. Saccade Based Audio Navigation

The higher level navigation scheme is split into two distinct phases: far field navigation and near field navigation, based on whether the MicroGlider is far away or near the sound source of interest respectively.

In far field navigation, the controller attempts to fly the MicroGlider directly towards the sound source, by minimizing the difference between the measured phase difference and the expected phase difference based on sensor placement (as is shown in Fig. 15).

When the MicroGlider detects that it is sufficiently close to the target, the controller switches to a saccade-based homing algorithm inspired by the navigation of real insects. In this scheme (shown in Fig. 16), the MicroGlider tries to constantly keep the sound source either on the right or left. This implies minimizing the phase difference detected between the two microphones. In this scheme, the aircraft flies without any navigation input (i.e in straight line segments) until either the optic flow sensor detects an obstacle or too high a phase difference between the two audio sensors is observed.

C. Optic Flow Architecture and Implementation

Obstacles will be detected and avoided with the use of optic flow sensing. Optic flow [8] is the apparent visual motion that results from relative motion between an imager (or eyeball) and other objects in the environment (Fig. 17). Consider an aircraft traveling in the forward direction. The

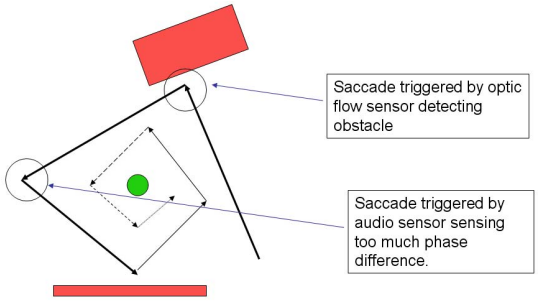

Fig. 16. Near field navigation scheme.

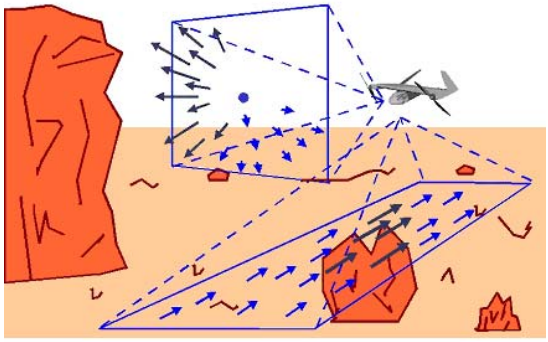

Fig. 17. Optic Flow, as seen from an aircraft.

ground will appear to move from front to back, with a rate that increases as the glider approaches the ground or as the glider flies over tall objects. Objects in front of the glider will grow in size, creating an expanding optic flow pattern. If the glider approaches a wall or tree line at an angle, the optic flow in the direction of that object will increase, indicating an imminent collision.

In order to integrate the imaging and image processing in a package suitable for inclusion on the MicroGlider, a custom "vision chip" for optic flow processing has been designed. A die photograph of the vision chip is shown in Fig. 18. The vision chip includes both image acquisition and low-level image processing on the same die. The vision chip architecture and circuitry is similar to that used in optic flow sensors developed by Barrows in earlier work [5]. The vision chip forms the focal plane of a camera-like imaging system. The image itself is formed by a lens or a pinhole. A 15-by-17 array of photoreceptors grabs a low-resolution image of the environment. An array of feature detectors, implemented with simple analog circuits, computes the presence of edges, saddle points, or other visual features in the visual field. The last layer of processing on the vision chip analyzes the feature detector outputs, and generates a single bit for each pixel. The bit is high or low indicating the presence or absence of a particular feature of interest. The optic flow processing is completed with a Microchip PIC 18LF2520, identical to the microcontroller used for controlling the MicroGlider. Optic flow is computed by tracking the motion of the high bit values generated by the vision chip. The optic flow sensor communicates with the power / control board (Fig. 13) using

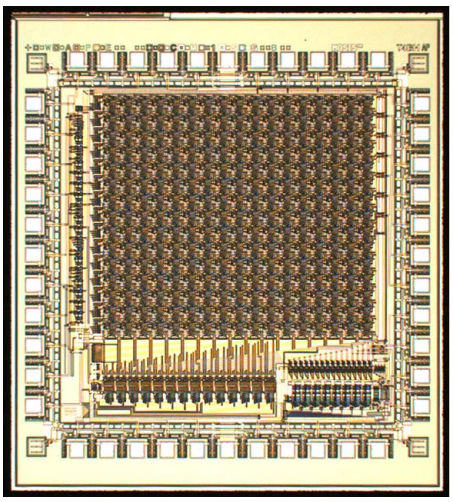

Fig. 18. Photograph of optic flow sensors vision chip.

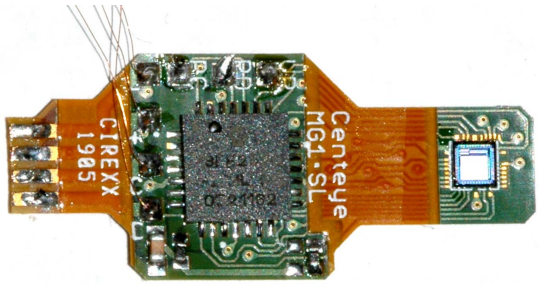

Fig. 19. 380mg optic flow sensor prototype.

the I2C serial interface built into these microcontrollers.

Earlier versions of these optic flow sensors have been fabricated in packages weighing 4.5 grams, which is clearly too heavy for the MicroGlider. However by using QFN-packaged PICs, extremely thin PC board material, and bare vision chip dies, we have been able to reduce the mass of a single optic flow sensor to 325 milligrams. Fig. 19 shows one prototype sensor, fabricated on the same flex-circuit material as the power / control board shown in Fig. 13.

Obstacle avoidance will be performed using various flight-control strategies observed in flying insects. The reader is referred to another paper [1] for a compilation of flight control strategies. Sample strategies include turning away from regions of high optic flow to avoid obstacles, equalizing optic flow on the left and right sides to fly down a corridors, and making zig-zag flight patterns to detect narrow objects.

V. Discussion

This paper has concentrated on the development of a set of core technologies key to the realization of an autonomous 2g glider. Future work will include closing the control loop for the audio sensors and the optic flow sensor to track a static audio source while avoiding obstacles.

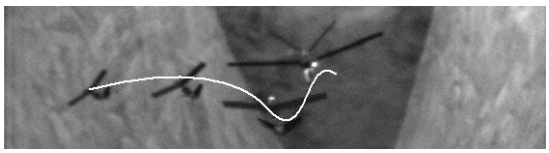

(a) Left turn

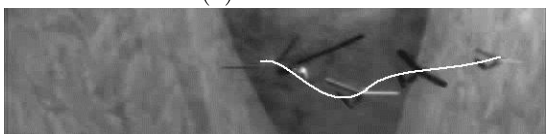

(b) Right turn

Fig. 20. Open loop left and right turns.

A. Integration

The five subsystems, control surfaces and fuselage, airfoil, control PCB, imager PCB, and battery are integrated together using molded short-fiber composite clips. This allows each piece to remain modular and its position with respect to the CG to be mutable. Once each subsystem is completed, the glider is attached to a low friction model aircraft balance and the position of each piece is selected to place the CG in the desired position (with respect to the roll and pitch axes). The effect of altering the CG can be observed with the flight simulator, however it is generally understood that it should be slightly forward and slightly below the center of lift for maximum stability and maneuverability.

B. Initial flight tests

To demonstrate the functionality of the MicroGlider, an open loop test was performed in a controlled laboratory environment. For this test a custom launch apparatus was constructed to ensure consistency in the initial flight conditions. The test was intended to demonstrate left and right turning capabilities. This was done by programming the microcontroller to first excite a roll, then a pitch. Sample flight sequences are shown in Fig. 20.

Acknowledgements

This material is based upon work supported by the National Science Foundation under Grant No. IIS-0412541. Any opinions, findings and conclusions or recommendations expressed in this material are those of the author(s) and do not necessarily reflect the views of the National Science Foundation (NSF). The authors also gratefully acknowledge DARPA for support under fund #FA8650-05-C-7138.

References

[1] Biologically inspired visual sensing and flight control. *The Aeronautical Journal of the Royal Aeronautical Society*, 107(1069), March 2003.

[2] P. Aarabi and S. Mavandadi. Robust sound localization using conditional timefrequency histograms. *Information Fusion*, 4:111–22, 2003.

[3] S. Avadhanula, R.J. Wood, D. Campolo, and R.S. Fearing. Dynamically tuned design of the MFI thorax. In *IEEE Int. Conf. on Robotics and Automation*, Washington, DC, May 2002.

[4] S. K. Banala, Y. Karakaya, S. McIntosh, Z. Khan, and S. K. Agrawal. Design and optimization of a mechanism for out of plane insect wing motion with twist. In *Proc. of DETC, ASME Design Engineering Technical Conferences*, Salt Lake City, Utah, September 2004.

[5] G. Barrows. *Fixed and Flapping Wing Aerodynamics for Micro Air Vehicle Applications*, volume 195 of *Progress in Astronautics and Aeronautics*, chapter 26. AIAA, 2001.

[6] J. Brufau, M. Puig-Vidal, J. López-Sánchez, J. Samitier, W. Driesen, J.M. Breguet, N. Snis, U. Simu, S. Johansson, and T. Velten. MICRON: Small autonomous robot for cell manipulation applications. In *IEEE Int. Conf. on Robotics and Automation*, Barcelona, Spain, April 2005.

[7] A. Cox, D. Monopoli, M. Goldfarb, and E. Garcia. The development of pizeoelectrically actuated micro-air vehicles. In *SPIE Conf. on Microrobotics and Microassembly*, volume 3834, pages 101–108, Boston, Massachusetts, September 1999.

[8] J.J. Gibson. *The Ecological Approach to Visual Perception*. Houghton Mifflin, Boston, MA, 1950.

[9] W.E. Green and P.Y. Oh. An aerial prototype for situational awareness in closed quarters. In *IEEE/RSJ Int. Conf. on Intelligent Robots and Systems*, pages 61–66, Las Vegas, Nevada, October 2003.

[10] E. Montane, P. Miribel-Catala, J. Lopez-Sanchez, M. Puig-Vidal, S. Bota, and J. Samitier. High-voltage smart power integrated circuits to drive piezoceramicactuators for microrobotic applications. *IEE Proc. Circuits, Devices & Systems*, 148(6):343–347, 2001.

[11] T.J. Mueller and J.D. DeLaurier. Aerodynamics of small vehicles. 35:89–111, 2003.

[12] E. Mumolo, M. Nolich, and G. Vercelli. Algorithms for acoustic localization based on microphone array in service robotics. *Robotics and Automation Systems*, 42:69 – 88, 2003.

[13] J.-D. Nicoud and J.-C. Zufferey. Towards indoor flying robots. In *IEEE/RSJ Int. Conf. on Intelligent Robots and Systems*, pages 787–792, Lausanne, Switzerland, October 2002.

[14] T. N. Pornsin, S. W. Lee, H. Nassef, J. Grasmeyer, Y. C. Tai, C. M. Ho, and M. Keennon. Mems wing technology for a battery powered ornithopter. In *The* 13_{th} *IEEE Anual Intl. Conf. on MEMS*, pages 709–804, Miyazaki, Japan, January 2000.

[15] T. N. Pornsin-shiriak, Y. C. Tai, H. Nassef, and C. M. Ho. Titanium-alloy MEMS wing technology for a micro aerial vehicle application. *J. of Sensors and Actuators A: Physical*, 89:95–103, March 2001.

[16] S. Sunada, T. Yasuda, K. Yasuda, and K. Kawachi. Comparison of wing characteristics at an ultralow reynolds number. *J. of Aircraft*, 39(2):331–338, 2002.

[17] R.J. Wood, S. Avadhanula, M. Menon, and R.S. Fearing. Microrobotics using composite materials: The micromechanical flying insect thorax. In *IEEE Int. Conf. on Robotics and Automation*, Taipei, Taiwan, September 2003.

[18] R.J. Wood, E. Steltz, and R.S. Fearing. Optimal energy density piezoelectric bending actuators. *J. of Sensors and Actuators A: Physical*, 119(2):476–488, 2005.

[19] J. Yan. *Design, Fabrication and Wing Force Control for a Micromechanical Flying Insect*. PhD thesis, University of California at Berkeley, December 2002.

[20] J. Yan, R.J. Wood, S. Avadhanula, and M. Sitti amd R.S. Fearing. Towards flapping wing control for a micromechanical flying insect. In *IEEE Int. Conf. on Robotics and Automation*, Seoul, Korea, May 2001.